

Signatures of fast and slow magnetohydrodynamic shocks in turbulent molecular clouds

Andrew Lehmann^{*} and Mark Wardle

Department of Physics and Astronomy, and Research Centre for Astronomy, Astrophysics & Astrophotonics, Macquarie University, Sydney, NSW 2109, Australia

8 November 2018

ABSTRACT

The character of star formation is intimately related to the supersonic magnetohydrodynamic (MHD) turbulent dynamics of the molecular clouds in which stars form. A significant amount of the turbulent energy dissipates in low velocity shocks. Fast and slow MHD shocks differ in how they compress and heat the molecular gas, and so their radiative signatures reveal distinct physical conditions.

We use a two-fluid model to compare one-dimensional fast and slow MHD shocks propagating at low speeds (a few km s^{-1}). Fast shocks are magnetically driven, forcing ion species to stream through the neutral gas ahead of the shock front. This magnetic precursor heats the gas sufficiently to create a large, warm transition zone where all the fluid variables smoothly change in the shock front. In contrast, slow shocks are driven by gas pressure, and neutral species collide with ion species in a thin hot slab that closely resembles an ordinary gas dynamic shock.

We consider shocks at velocities $v_s = 2\text{--}4 \text{ km s}^{-1}$ and preshock Hydrogen nuclei densities $n_{\text{H}} = 10^2\text{--}10^4 \text{ cm}^{-3}$. We include a simple oxygen chemistry and cooling by CO, H₂ and H₂O. CO rotational lines above $J = 6 \rightarrow 5$ are more strongly excited in slow shocks. These slow shock signatures may have already been observed in infrared dark clouds in the Milky Way.

Key words: MHD – shock waves – turbulence – ISM: clouds – submillimetre: ISM

1 INTRODUCTION

Understanding the internal environment of the giant molecular clouds (GMCs) in which stars form is a necessary precursor to addressing the star formation rate and stellar initial mass function (e.g., Bergin & Tafalla 2007; McKee & Ostriker 2007). Large non-thermal linewidths observed in molecular lines (e.g., Larson 1981; Solomon et al. 1987) have often been attributed to turbulent motions. Furthermore, the kinetic energy associated with these motions is generally found to be on the order of the gravitational potential energy, indicating the importance of turbulence as a dynamical component of molecular clouds. In addition, magnetic fields in GMCs give Alfvén velocities on the order of the observed velocity dispersions (e.g., Crutcher et al. 1993; Crutcher 1999; Crutcher et al. 2010). This suggests that the turbulence in GMCs is magnetohydrodynamic (MHD) in nature.

The physics underlying the MHD turbulence of molecular clouds is intimately connected with properties of

star formation (Mac Low & Klessen 2004). For example, Federrath & Klessen (2012) and Federrath & Klessen (2013) use three dimensional MHD simulations to analyse different modes of turbulence by comparing compressive driving to solenoidal driving. They showed that the star formation rate and efficiency are both sensitive to these driving modes and Mach number variations. Hence it is desirable to discover observable distinctions between different modes of turbulence.

Supersonic turbulence dissipates via shock waves and vortices (Pety & Falgarone 2000). In simulations of compressible MHD turbulence Stone et al. (1998) found that shock waves dissipated 50% of the turbulent energy in a strong magnetic field model and 32% in a weak field model. The heating of compressed gas in a thin post-shock region uniquely drives chemistry and radiative cooling. Thus the radiative characteristics of turbulent dissipation will be strongly shaped by cooling in shocks. Furthermore, Smith et al. (2000b) found that weak shocks in a large range of velocities were responsible for the majority of dissipation in simulations of decaying MHD turbulence. In contrast, a small range of stronger shocks dissipated turbulence

^{*} E-mail: andrew.lehmann@mq.edu.au

that was being driven (Smith et al. 2000a). Hence radiative signatures of shocks could be used to distinguish between these two scenarios.

The observational signatures of the low-velocity shocks that dominate dissipation of MHD turbulence have only recently been considered. Pon et al. (2012) considered C-type fast MHD shocks travelling at speeds of $2\text{--}3\text{ km s}^{-1}$ perpendicular to the magnetic field and computed the abundances and emission of H_2 , CO and H_2O . By comparing CO rotational line emission from these shocks to those produced in photodissociation regions (PDRs), they found that fast shocks dominate the emission in transitions above $J = 5 \rightarrow 4$. Lesaffre et al. (2013) take a statistical approach by computing observational diagnostics due to a distribution of C- and J-type fast, perpendicular, MHD shocks at velocities ranging from $3\text{--}40\text{ km s}^{-1}$. They use these shocks to explain the radiation from a turbulent wake formed by a galaxy collision in Stephan’s Quintet.

Anomalously bright CO lines above $J = 5 \rightarrow 4$ have been recently observed towards Milky Way molecular clouds (e.g., Pon et al. 2014, 2015; Larson et al. 2015) and from warm molecular gas in external galaxies (e.g., Kamenetzky et al. 2012; Pellegrini et al. 2013). These studies all conclude that PDR models are unable to reproduce the bright high- J CO lines and all suggest MHD shock waves as the heating mechanism. The shock models used or referred to in these studies (Flower & Pineau Des Forêts 2010; Pon et al. 2012) and other studies of shocks in interstellar clouds (e.g. Draine & Katz 1986; Hollenbach & McKee 1989; Chapman & Wardle 2006) all consider *fast* MHD shocks. MHD fluids can, however, support three kinds of shocks: fast, intermediate and slow. Unfortunately no study has identified which kinds of shocks would be produced by MHD turbulence. One of the goals of our work is to motivate the classification of MHD shocks in turbulent molecular clouds.

Ideal MHD assumes a fully ionized gas in which the magnetic field is frozen. Molecular clouds are in fact only weakly ionized and the magnetic field acts on the neutral fluid via the ionized fluid. A two-fluid description is therefore more appropriate to molecular cloud studies. Early work by Lithwick & Goldreich (2001) and Lazarian et al. (2004) highlighted the importance of two-fluid effects on the turbulent cascade. Recently it has become feasible to run high resolution three dimensional two-fluid MHD simulations. For example, Meyer et al. (2014) use simulations to show that observations of linewidth differences between line emission from neutral and ion species can be accounted for by two-fluid effects. Furthermore, Burkhart et al. (2015) use simulations to show that the Alfvénic modes do not necessarily dissipate at the ambipolar diffusion scale. They also confirm the analytic results of Balsara (1996) and Tilley & Balsara (2011) that in molecular cloud conditions, the fast and Alfvén modes are strongly damped by ion-neutral collisions leaving the slow modes to propagate with little damping. Thus nonlinear steepening into slow shocks might be expected to preferentially occur in molecular clouds. In addition, slow shocks reach far higher peak temperatures than fast shocks for two reasons. Firstly, the heating timescale in fast shocks is determined by the long ion-neutral collision timescale while in slow shocks is determined by the short neutral-ion collision timescale. As the cooling timescale of

the gas lies between these two, the gas being overrun by fast shocks remains at low temperatures whereas it quickly heats up within slow shocks. Secondly, as we show in Section 2 the gas in fast shocks necessarily loses some of its kinetic energy to strengthening the magnetic field while in slow shocks it does not. Thus slow shocks have more energy available to heat the gas.

In this paper, we solve the steady, plane parallel two-fluid MHD equations to model shocks that propagate at any angle to the magnetic field. In Section 2 we elucidate some of the basic differences of fast and slow MHD shocks. We describe our computational scheme in Section 3. In Section 4 we compare fast and slow shocks in the low-velocity regime with molecular cloud conditions. We discuss their radiative characteristics and implications for interpreting emission from turbulent molecular gas. Finally, in Section 5 we show how these signatures might be used to interpret observations.

2 THEORY

Cosmic rays streaming through the interstellar medium weakly ionize molecular clouds, generating an ion fluid that interpenetrates the neutral particles. A two-fluid MHD description is developed in Section 2.1 with the ion fluid coupled to the magnetic field via the Lorentz force and to the neutral fluid via the collisional force, so that

$$\frac{\mathbf{J} \times \mathbf{B}}{c} = \alpha \rho_i \rho_n (\mathbf{v}_i - \mathbf{v}_n)$$

where α is the rate coefficient for elastic ion-neutral scattering and ρ and \mathbf{v} are the density and velocity with subscripts i and n referring to ion and neutral fluids respectively. By considering the state of these fluids far away from the shock front, we illustrate how the various families of MHD shocks come about and highlight the different effects they have on the ambient magnetic field.

A simplified chemical model, in which two body reactions and photodissociation affect the abundances of coolants, is presented in Section 2.2. Finally, the details of how those coolants radiate are outlined in Section 2.3. Only rotational excitations of molecular species are considered because vibrational excitations do not become significant until temperatures reach $\gtrsim 1000\text{ K}$, which are not achieved in the low velocity shocks computed here.

2.1 Two-Fluid MHD

Conservation equations

While turbulence is an inherently three-dimensional problem (e.g. Burkhart et al. 2015, and references therein), shock waves are extremely thin structures within a turbulent system. Hence we follow Draine (1986) by considering a stationary plane-parallel shock travelling in the z direction with the magnetic field initially lying in the $x\text{--}z$ plane. The governing

equations of the ion fluid are

$$\frac{d}{dz} (\rho_i v_{iz}) = 0, \quad (1)$$

$$\frac{d}{dz} \left(\frac{B_z B_x}{4\pi} \right) = \alpha \rho_i \rho_n (v_{ix} - v_{nx}), \quad (2)$$

$$\frac{d}{dz} \left(\frac{B_x^2}{8\pi} \right) = -\alpha \rho_i \rho_n (v_{iz} - v_{nz}). \quad (3)$$

The neutral fluid equations are

$$\frac{d}{dz} (\rho_n v_{nz}) = 0, \quad (4)$$

$$\frac{d}{dz} (\rho_n v_{nz} v_{nx}) = \alpha \rho_i \rho_n (v_{ix} - v_{nx}), \quad (5)$$

$$\frac{d}{dz} (\rho_n v_{nz}^2 + P_n) = \alpha \rho_i \rho_n (v_{iz} - v_{nz}), \quad (6)$$

$$v_{nz} \frac{dP_n}{dz} + \gamma P_n \frac{dv_{nz}}{dz} = (\gamma - 1) (\Gamma - \Lambda) \quad (7)$$

where P_n is the neutral pressure, Γ is the heating function, Λ is the cooling function, and the internal energy $u = P_n / (\gamma - 1)$ for adiabatic index γ . Finally, the electromagnetic equations give

$$\frac{d}{dz} (v_{iz} B_x - v_{ix} B_z) = 0, \quad (8)$$

$$\frac{d}{dz} (B_z) = 0. \quad (9)$$

Solving for the internal structure of intermediate shocks requires equations analogous to Equations (2) to (9) for the y -direction. We consider only fast and slow shocks here by ignoring this case. Far away from the shock front there is no velocity difference between the fluids. This means there is no frictional heating in those regions, and so the shocks satisfy the isothermal one-fluid jump conditions. The types of shocks allowed are therefore determined by the MHD signal speeds.

Shock Families

When considering small perturbations of density, pressure, the velocity field, and the magnetic field around time independent averages the equations of MHD allow for three linear wave modes: the fast, intermediate and slow waves. These waves travel with phase velocities

$$f = \left(\frac{v_A^2 + c_s^2}{2} + \frac{1}{2} \sqrt{(v_A^2 + c_s^2)^2 - 4v_A^2 c_s^2 \cos^2 \theta} \right)^{1/2},$$

$$i = v_A \cos \theta,$$

$$s = \left(\frac{v_A^2 + c_s^2}{2} - \frac{1}{2} \sqrt{(v_A^2 + c_s^2)^2 - 4v_A^2 c_s^2 \cos^2 \theta} \right)^{1/2},$$

where $v_A = B / \sqrt{4\pi\rho}$ is the Alfvén velocity, $c_s = \sqrt{k_B T / \mu_m}$ is the isothermal sound speed with Boltzmann constant k_B and mean mass per particle $\mu_m = (7/3) m_H$, and θ is the angle between the magnetic field and the direction of propagation under consideration. These speeds are plotted as functions of θ in Figure 1 for the case $v_A > c_s$ (the relevant case in molecular clouds).

In the frame of reference comoving with a shock front, the preshock fluid travels toward the shock front at a shock velocity v_s greater than one of the wave speeds. The three wave speeds demarcate four regions of fluid velocities

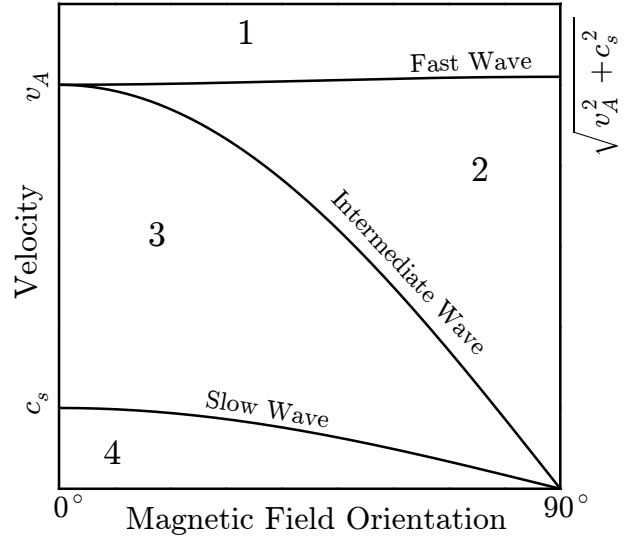


Figure 1. The phase velocities of linear MHD wave modes versus the angle between the magnetic field and direction of propagation of those modes for $v_A > c_s$. The wave speeds delineate the regions marked 1 to 4.

marked 1 to 4 in Figure 1. Inside of the shock front the fluid must transition down across a wave speed, which allows for six kinds of shock waves collected into three families: fast, intermediate and slow MHD shocks. Fast shocks are those that cross the fast wave speed only (1 \rightarrow 2), intermediate shocks cross the intermediate wave speed (1 \rightarrow 3, 1 \rightarrow 4, 2 \rightarrow 3 and 2 \rightarrow 4), and slow shocks cross the slow wave speed only (3 \rightarrow 4).

Far ahead and far behind a shock where there is no friction between the fluids—and hence $\mathbf{v}_n = \mathbf{v}_i$ —one can show from Equations (1) to (9) that the product

$$\left(\frac{v_z^2 - i^2}{v_z} \right) B_x$$

is conserved across any shock. This can be used to emphasise some basic differences between the different kinds of shocks. Suppose, for simplicity that $B_x > 0$ in the preshock medium. Recall that a fast shock crosses the fast wave speed only, so that the term in parentheses remains positive but is reduced across the shock. Thus B_x must increase to compensate. In intermediate shocks, the velocity crosses the intermediate wave speed and so the term in parentheses switches sign across the shock. This implies that B_x must switch sign also. Finally, in slow shocks, the velocity crosses the slow wave speed only, so that the term in parentheses is negative and becomes further negative in the postshock medium. This means that B_x must decrease to compensate. These three effects on the magnetic field direction are shown schematically in Figure 2.

The switch in sign of B_x in the intermediate shock is due to a rotation of the magnetic field within the shock front. As the field rotates out of the x - z plane, intermediate shocks require equations analogous to Equations (2) to (9) for the y -direction. This case is ignored here because it is unclear whether steady state intermediate shocks are physically admissible (e.g., Wu 1987; Falle & Komissarov 2001). Furthermore, the 1 \rightarrow 3 intermediate shock will resemble a

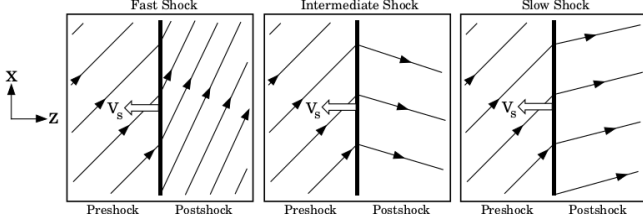


Figure 2. The effect on magnetic field orientation of the three classes of MHD shock waves. Fast shocks (left) increase the angle between the field and shock normal, intermediate shocks (middle) reverse the sign of the angle and slow shocks (right) decrease it.

fast shock as it crosses the fast speed, the heating in a $2 \rightarrow 4$ shock front will be dominated by a hydrodynamic jump as it crosses the sound speed—see Section 3—and thus resemble a slow shock, the $2 \rightarrow 3$ shock will only weakly heat the gas as it resembles a rotational discontinuity, and finally the $1 \rightarrow 4$ shock will resemble a fast shock followed by a weak $2 \rightarrow 3$ shock followed by a slow shock, so our models should also roughly capture its structure (Kennel et al. 1989).

As the spacing of field lines is proportional to the magnetic field strength, one can see in Figure 2 that the field strength increases across fast shocks and decreases across slow shocks. This means that some of the kinetic energy of a fast shock is converted into magnetic field energy. Hence, for slow shocks at the same velocity one expects there to be more energy available to heat the gas.

Governing Differential Equations

With some manipulation, Equations (1) to (9) reduce to three ordinary differential equations determining changes in the x component of the magnetic field and the neutral fluid temperature:

$$\frac{dB_x}{dz} = \frac{v_s^2 \alpha \rho_{i0} B_0^2}{v_A^2 B_z} \left(\frac{v_{ix} - v_{nx}}{v_{nz} v_{iz}} \right), \quad (10)$$

$$\frac{dT_n}{dz} = \frac{T_n (\gamma - 1)}{\rho_{n0} v_s^3 (v_{nz}^2 - \gamma \tau v_s^2)} \times \left(\left(\frac{v_{nz}^2}{\tau} - v_s^2 \right) (\Gamma - \Lambda) - \alpha \rho_i \rho_n (v_{iz} - v_{nz}) v_{nz} v_s^2 \right) \quad (11)$$

with the velocities

$$\begin{aligned} v_{nx} &= \frac{v_A^2 B_z}{v_s B_0^2} (B_x - B_{x0}), \\ v_{ix} &= \frac{v_{iz} B_x - v_s B_{x0}}{B_z}, \\ v_{nz} &= \frac{v_s}{2} \left(\beta \pm \sqrt{\beta^2 - 4\tau} \right), \\ v_{iz} &= \frac{v_s B_{x0} B_x + B_z (B_x v_{nx} + B_z v_{nz})}{B_0^2}, \end{aligned}$$

the preshock Alfvén velocity

$$v_A = \frac{B_0}{\sqrt{4\pi\rho_{n0}}}$$

and

$$\begin{aligned} \beta &= 1 + \frac{k_B T_{n0}}{\mu_m v_s^2} + \frac{1}{2} \frac{v_A^2 B_{x0}^2 - B_x^2}{v_s^2 B_0^2}, \\ \tau &= \frac{k_B}{\mu_m v_s^2} T_n \end{aligned}$$

where a subscript 0 denote preshock values.

Equations (10) and (11) are not complete without specifying how energy leaves the gas via Λ and enters via Γ . The collisions between the ion and neutral fluids generate frictional heating at a rate

$$\Gamma_F = \alpha \rho_n \rho_i (\mathbf{v}_i - \mathbf{v}_n)^2.$$

per unit volume. In addition, we include cosmic-ray heating, which is only important at temperatures of 10–30 K.

The shock heated gas cools by radiating away heat energy stored in the rotational and vibrational modes of its constituents. These modes are collisionally excited, so that the cooling function must be a function of the densities of the coolants, the density of the colliding particles and the temperature of the gas. The abundances of coolants can change due to chemical reactions, and so we present a simple model for the oxygen chemistry occurring in the shock heated gas in the next section before specifying how that gas radiates in Section 2.3.

2.2 Chemistry

Radiative cooling depends on the the abundances of the coolants and hence chemical reactions influence the cooling of the gas. The dominant coolants in molecular clouds are CO, H₂ and H₂O (e.g., Neufeld & Kaufman 1993) and the abundance of the latter is determined in this study by the set of eight reactions listed in Table 1, adopted from Wagner & Graff (1987). Previous models of the gas phase chemistry in interstellar environments—using more than 100 reactions—were found to be dominated by a small set of reactions (e.g., Iglesias & Silk 1978). The reactions of Wagner & Graff are the subset of these dominant reactions that control the abundance of H₂O.

The change in the particle density of a neutral species M through the shock is given by

$$\frac{d}{dz} (n(M) v_{nz}) = S_M$$

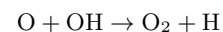
where S_M is the rate at which M is created or destroyed. $\sum S_M$ over all neutral species must be zero in order for Equation (4) to remain true. The low densities of molecular clouds mean that only two body chemical reactions and photodissociation processes need to be considered. Two-body reaction rates between species A with particle density $n(A)$ and species B with particle density $n(B)$ take the form

$$k_{AB}(T) n(A) n(B) \text{ cm}^{-3} \text{ s}^{-1}$$

where $k_{AB}(T)$ is a rate coefficient. The UMIST Database for Astrochemistry 2012 (RATE12) (McElroy et al. 2013) gives this coefficient in the form

$$k_{AB}(T) = \alpha \left(\frac{T}{300} \right)^\beta \exp \left(-\frac{\gamma}{T} \right) \text{ cm}^3 \text{ s}^{-1}$$

where α , β and γ are constants. The values of these parameters for the reactions used are shown in Table 1. These rates are verified for the temperature range 200 – 2500 K, so there is some uncertainty when extrapolating down to 10 K. In fact, for the reaction



the rate coefficient parameters in the RATE12 database give

Table 1. Reaction rate coefficient parameters.

No.	Reaction	α	β	γ
1	$\text{O} + \text{H}_2 \rightarrow \text{OH} + \text{H}$	3.14×10^{-13}	2.70	3150.0
2	$\text{OH} + \text{H} \rightarrow \text{O} + \text{H}_2$	6.99×10^{-14}	2.80	1950.0
3	$\text{OH} + \text{H}_2 \rightarrow \text{H}_2\text{O} + \text{H}$	2.05×10^{-12}	1.52	1736.0
4	$\text{H}_2\text{O} + \text{H} \rightarrow \text{OH} + \text{H}_2$	1.59×10^{-11}	1.20	9610.0
5	$\text{OH} + \text{OH} \rightarrow \text{H}_2\text{O} + \text{O}$	1.65×10^{-12}	1.14	50.0
6	$\text{H}_2\text{O} + \text{O} \rightarrow \text{OH} + \text{OH}$	1.85×10^{-11}	0.95	8571.0
7	$\text{O} + \text{OH} \rightarrow \text{O}_2 + \text{H}$	4.33×10^{-11}	-0.5	30.0
8	$\text{O}_2 + \text{H} \rightarrow \text{O} + \text{OH}$	2.61×10^{-10}	0	8156.0

Notes. The parameters for reaction 7 are taken from Wagner & Graff (1987) instead of RATE12.

a rate that diverges in the 10–100 K range. For this rate the parameters are taken from Wagner & Graff (1987). In Figure 3, the rates are plotted against temperature. It can be seen that most of the rates only “turn on” at temperatures $T \gtrsim 60$ K, which is why the weak fast shocks considered here only negligibly affect the molecular abundances.

Photodissociation in molecular clouds is caused by ultraviolet radiation generated by secondary electrons in cosmic ray ionization events (?). The rates of photodissociation events per volume of species A with particle density $n(A)$ take the form

$$p_A \frac{\zeta_{CR}}{1-\omega} n(A) \text{ cm}^{-3} \text{ s}^{-1}$$

where ζ_{CR} is the cosmic ray ionization rate, ω is the albedo of the dust grains found in molecular clouds and p_A is an efficiency constant. The ionization rate ζ_{CR} is set to 10^{-17} s^{-1} , the albedo w is set to 0.6, and the values of p_A for the reactions considered—taken from Gredel et al. (1989)—are shown in Table 2.

With these two rates and using the static, planar assumptions the abundance of species M relative to the hydrogen nuclei density $x_M = n(M)/n_H$ changes as

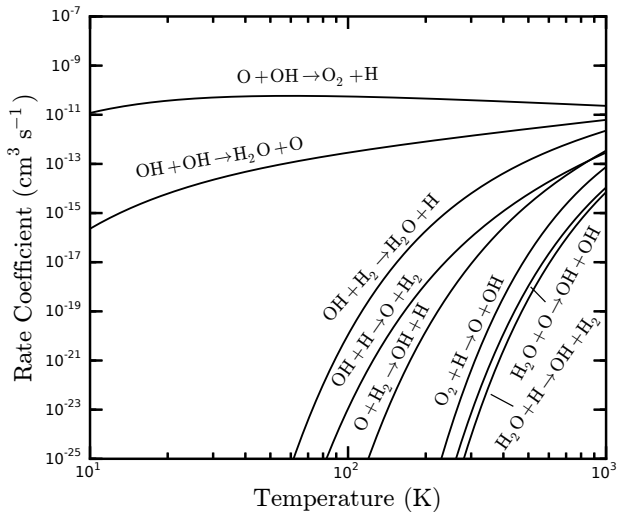
$$\frac{d}{dz}(x_M) = \frac{n_H^2}{n_0 v_s} \left(\sum k_{AB}(T)x(A)x(B) + \sum p_A \frac{\zeta_{CR}}{1-\omega} x(A) \right)$$

where n_0 is the preshock H-nuclei density and the sums are taken over reactions that either produce or destroy M .

The end result of this chemistry is to add five more differential equations—coupled to each other through densities and to Equations (10) and (11) through temperature—to follow the abundances of H, O, OH, O_2 and H_2O . We follow Pon et al. (2012) in using an initial H_2O abundance of 10^{-7} , O abundance of 5.45×10^{-4} and a C abundance of 1.4×10^{-4} which is assumed to be entirely locked up in CO. The CO abundance is assumed to be constant throughout the shock, because it has a dissociation temperature higher than any temperature reached in these weak shocks. The initial H, OH and O_2 abundances are set to 10^{-4} , 10^{-12} and 10^{-10} respectively. H_2 abundance is then computed through the shock using $x_{\text{H}_2} = (1/2)(1 - x_H)$.

2.3 Cooling

The cooling function of Neufeld & Kaufman (1993) is adopted for this model. This uses an escape probability to account for the effects of reabsorption by the surrounding

**Figure 3.** Reaction rate coefficients as a function of temperature.**Table 2.** Photodissociation rate efficiency.

Reaction	p_A
$\text{H}_2\text{O} + \text{Photon} \rightarrow \text{OH} + \text{H}$	971
$\text{OH} + \text{Photon} \rightarrow \text{O} + \text{H}$	509
$\text{O}_2 + \text{Photon} \rightarrow \text{O} + \text{O}$	751

Notes. Photodissociation rate efficiencies taken from Gredel et al. (1989).

media on the rotational level populations. Collisions with H_2 are the only excitations considered as the abundance of H_2 in molecular clouds is orders of magnitude above the next most abundant molecular species. The power radiated by CO, H_2O and H_2 in a wide range of conditions is expressed in terms of a rate coefficient L_M defined such that the power radiated per unit volume by species M is

$$\Lambda_M = n(M)n(\text{H}_2)L_M.$$

L_M is a function of H_2 density, temperature and an optical depth parameter $\tilde{N}(M)$. $\tilde{N}(M)$ is a correction factor that accounts for reabsorption of radiation by the same molecule in the surrounding gas. It depends on the geometry of the system in question, the density of M and the local velocity gradient. The expression for a plane-parallel slab of thickness d and characteristic velocity difference Δv ,

$$\tilde{N}(M) = \frac{n(M)d}{9\Delta v}, \quad (12)$$

is used here. L_M is then expressed with a four parameter analytic fit to its density dependence

$$\frac{1}{L_M} = \frac{1}{L_0} + \frac{n(\text{H}_2)}{L_{LTE}} + \frac{1}{L_0} \left(\frac{n(\text{H}_2)}{n_{1/2}} \right)^\alpha \left(1 - \frac{n_{1/2}L_0}{L_{LTE}} \right)$$

where L_0 is the low density limit of the cooling rate coefficient, L_{LTE} is the luminosity per molecule with the level population in local thermodynamic equilibrium and $n_{1/2}$ is the H_2 density at which the cooling rate coefficient is half of L_0 . L_0 is a function of temperature only while L_{LTE} , $n_{1/2}$ and α are functions of temperature and $\tilde{N}(M)$.

Preliminary isothermal shocks were computed in order to gain an estimate on the values of d and Δv , and these values checked for self consistency against the results when cooling was included. The average value of $n(M)$ through the shock was used. H_2 is optically thin in all interesting astrophysical conditions, so L_{H_2} does not depend on Equation (12).

The values of L_0 , L_{LTE} , $n_{1/2}$ and α for CO, H_2O and H_2 are taken from Neufeld et al. (1995) in the temperature range $T = 10\text{--}100$ K, and from Neufeld & Kaufman (1993) in the range $T = 100\text{--}2000$ K. We combine the parameters in the $T = 10\text{--}100$ K range using an ortho-to-para H_2O ratio of 3:1, which was already assumed in the $T = 100\text{--}2000$ K range. The values of some of these parameters at $T = 100$ K are inconsistent between the two sources, so we take the mean value.

3 NUMERICAL INTEGRATION

The core of this problem are the first order ordinary differential equations which take the form:

$$\begin{aligned}\frac{dB_x}{dz} &= f_1(z, B_x, T) \\ \frac{dT}{dz} &= f_2(z, B_x, T)\end{aligned}$$

for f_1 and f_2 defined by Equations (10) and (11). They must be solved simultaneously with the abundance derivatives which are coupled to these two through their dependence on temperature. When supplied with initial conditions, these equations can be integrated to give B_x , T and the abundances as functions of z . The open source *PYTHON* module *scikits.odes*¹ was used, which solves initial value problems for ODEs using variable-order, variable-step, multistep methods.

The initial conditions are stationary states—in that their z derivatives are zero—so integrating from these points changes nothing. A perturbation must be added to these initial conditions in the form

$$\begin{aligned}B_x &= B_{x0} + \delta B_x e^{\lambda_x z} \\ T &= T_0 + \delta T e^{\lambda_T z}\end{aligned}$$

before integrating. The effect of the perturbation can be understood by linearising the differential equations (10) and (11). It is illuminating to look at the isothermal case—where $\gamma = 1$ —so that only the B field derivative remains. In this case we get the eigenvalue

$$\lambda_x = \frac{\alpha \rho_{i0}}{v_s} \frac{(v_s^2 - f^2)(v_s^2 - s^2)}{v_A^2 (v_s^2 - c_s^2)}$$

where f , i and s are the fast, intermediate and slow signal speeds defined in Section 2.1. λ_x determines whether the perturbation of B_x grows or decays. By replacing the preshock variables with their postshock counterparts, the eigenvalue can also be used to explore the region of solution space near postshock states.

For fast shocks, the preshock state is in region 1 of Figure 1 so that $v_s > f > i > c_s > s$. This means λ_x is

positive so that B_x grows. This describes an unstable stationary point, where any perturbation away from the initial condition grows. The postshock state is in region 2 so that $f > v_f > i > c_s > s$ where v_f is the final velocity. This means λ_x is negative so that this state is a stable stationary point. In Section 2.1, we noted that the fast shock increases B_x , hence a positive perturbation of the initial B_x is all that is required to finish at the fast postshock state.

For slow shocks, the preshock state is in region 3 of Figure 1 so that $f > i > v_s > c_s > s$ in the supersonic case. This means λ_x is negative and this state is a stable stationary point. Hence there is no way to leave the supersonic slow preshock state in a continuous fashion like in C-type fast shocks. The slow solution is further complicated by a singularity in the equations when crossing the sound speed ($v_{nz} \rightarrow c_s$), as a manipulation of Equation (7) gives

$$\frac{dv_{nz}}{dz} = \frac{(\gamma - 1)(\Gamma - \Lambda) - \alpha \rho_n \rho_i (v_{iz} - v_{nz}) v_{nz}}{\rho_n (c_s^2 - v_{nz}^2)}.$$

We cross this sonic point by inserting a gas dynamic jump in the neutrals determined by the hydrodynamic jump conditions:

$$\frac{v_2}{v_1} = \frac{\gamma - 1}{\gamma + 1} + \frac{2}{\gamma + 1} \frac{1}{M^2} \quad (13)$$

$$\frac{T_2}{T_1} = \left(1 + \frac{2\gamma}{\gamma + 1} (M^2 - 1)\right) \frac{M^2 (\gamma - 1) + 2}{M^2 (\gamma + 1)} \quad (14)$$

where $M^2 = \rho_1 v_1^2 / \gamma P_1$ and v_2 and T_2 are the neutral z velocity and temperature immediately after the gas dynamic jump. The slow postshock state lies in region 4 of Figure 1 so that $f > i > c_s > s > v_f$ and λ_x is negative. This means this state is a stable stationary point, and so jumping across the sound speed (via Equation (13)) will allow the solution to smoothly settle onto the slow postshock state.

For slow shocks with a subsonic preshock state, $f > i > c_s > v_s > s$ so that λ_x is positive and the stationary state is an unstable. This means a perturbation that reduces B_x will grow smoothly until the solution reaches the slow postshock state. Such a shock is a C-type slow MHD shock, and will be ignored here because it requires high sound speeds and therefore high temperatures that are not obviously relevant for molecular cloud studies.

4 RESULTS

Here we compare a set of shock models with parameters shown in Table 3. The turbulent cascade of energy ensures the dissipation is dominated by low-velocity shocks, so we follow Pon et al. (2012) in looking at velocities around 3 km s^{-1} . In Figure 4, the Alfvén velocity is plotted against the magnetic field orientation θ with dashed lines of constant intermediate speed $i = v_A \cos \theta$ overlaid. The magnetic field strength on the second vertical axis is computed for a preshock density $n_0 = 10^3 \text{ cm}^{-3}$. The intermediate speed is the upper bound of possible slow shock velocities—region 3 in Figure 1—and so the dashed lines in Figure 4 trace the minimum field strength required to get slow shocks with peak temperatures shown. We thus chose θ low enough to retain reasonable field strength values. At $\theta = 30^\circ$, a 4 km s^{-1} slow shock—which will heat the gas to $\sim 857 \text{ K}$ immediately after the neutral jump—requires an Alfvén velocity of

¹ <https://github.com/bmcage/odes>

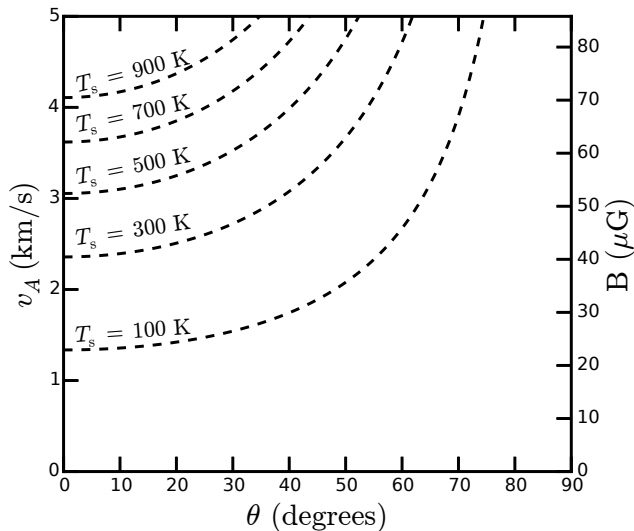


Figure 4. Alfvén velocity versus magnetic field orientation, with dashed lines of constant intermediate speed $v_A \cos \theta$ that allow slow MHD shocks to reach the peak temperatures shown. The magnetic field strength on the second vertical axis assumes preshock density $n_0 = 10^3 \text{ cm}^{-3}$.

$\sim 4.6 \text{ km s}^{-1}$, which is fixed for all the slow shocks at different preshock densities. This gives magnetic field strengths in the range $B_0 = 25\text{--}253 \text{ }\mu\text{G}$. Finally, \tilde{N} was initially chosen for preliminary isothermal shocks, and then recomputed after each shock model for consistency. Table 3 shows the self consistent values of $\tilde{N}(\text{CO})$ and $\tilde{N}(\text{H}_2\text{O})$.

Structural characteristics

In Figures 5 and 6 we compare fast and slow shock profiles of ion and neutral velocity, density, temperature, cooling rate and abundances for $v_s = 3 \text{ km s}^{-1}$. The fast shock propagates at 89.9° to a $10 \text{ }\mu\text{G}$ magnetic field, while the slow shock propagates at 30° to an $80 \text{ }\mu\text{G}$ field. The preshock density $n_0 = 10^3 \text{ cm}^{-3}$ for both.

In the velocity profiles—upper panels of Figures 5 and 6—the neutral and ion velocities in the shock propagation direction are the dashed and dotted lines respectively. These plots are in the frame of reference of the shock wave, and so velocities below the shock velocity represent fluid flowing ahead of the shock front in the lab frame, in which the shock wave travels to the left. Therefore, in the fast shock the ions stream ahead, imparting some of their momentum to the neutrals until both fluids are moving at the same speed in the postshock medium (on the right side of each plot). This process is set by the long ion-neutral collision timescale and therefore happens smoothly over a large distance, and there is no viscous jump as seen in hydrodynamic shocks. In contrast, for the slow shock it is the neutrals that flow ahead of the ions that then get accelerated to the neutral velocity over a small distance—set by the fast neutral-ion collision timescale—giving slow shocks a much thinner structure than the fast shocks. The cooling timescale of the gas lies between the two collision timescales, and so slow shocks will reach higher peak temperatures than fast shocks at the same velocity.

Table 3. Shock Parameters.

Parameters	v_s km/s	$\log \tilde{N}(\text{CO})$ $\log(\text{cm}^{-2} (\text{km/s})^{-1})$	$\log \tilde{N}(\text{H}_2\text{O})$
Fast Shocks, $\theta = 89.9^\circ$			
$n_0 = 10^2 \text{ cm}^{-3}$	2.0	15.9	11.7
$B_0 = 3 \text{ }\mu\text{G}$	2.5	15.7	11.8
	3.0	15.6	11.9
	3.5	15.5	11.9
	4.0	15.5	11.9
$n_0 = 10^3 \text{ cm}^{-3}$	2.0	15.8	12.7
$B_0 = 10 \text{ }\mu\text{G}$	2.5	15.8	12.7
	3.0	15.8	12.6
	3.5	15.8	12.6
	4.0	15.5	12.3
$n_0 = 10^4 \text{ cm}^{-3}$	2.0	15.9	12.8
$B_0 = 32 \text{ }\mu\text{G}$	2.5	15.8	12.7
	3.0	15.8	12.8
	3.5	15.7	12.6
	4.0	15.7	12.6
Slow Shocks, $\theta = 30^\circ$			
$n_0 = 10^2 \text{ cm}^{-3}$	2.0	14.5	11.0
$B_0 = 25 \text{ }\mu\text{G}$	2.5	14.5	11.0
	3.0	14.5	11.0
	3.5	14.5	11.4
	4.0	14.5	12.3
$n_0 = 10^3 \text{ cm}^{-3}$	2.0	14.5	11.0
$B_0 = 80 \text{ }\mu\text{G}$	2.5	14.5	11.0
	3.0	14.5	11.5
	3.5	14.5	12.6
	4.0	14.5	13.2
$n_0 = 10^4 \text{ cm}^{-3}$	2.0	15.6	12.6
$B_0 = 253 \text{ }\mu\text{G}$	2.5	15.7	12.7
	3.0	15.1	13.6
	3.5	15.0	14.6
	4.0	15.0	15.1

The density profiles—solid black lines in the upper panels—similarly show large differences between the shocks. The fast shock weakly compresses the gas by a factor of ~ 7 in a simple, smooth manner. The slow shock has a complex density profile that ends with a compression ratio of ~ 300 and must be understood in conjunction with the temperature and cooling (see middle panel) taking place. It starts with the neutral jump, governed by Equations (13) and (14), compressing the gas by a factor of ~ 4 and heating it to $\sim 500 \text{ K}$. Combining Equations (3) and (6) we get

$$\frac{d}{dz} \left(\rho_n v_{nz}^2 + P_n + \frac{B^2}{8\pi} \right) = 0$$

where we identify each term as effective pressure terms: ram pressure $P_{ram} = \rho_n v_{nz}^2$, gas pressure $P_{gas} = P_n = nk_B T$ and magnetic pressure $P_{mag} = B^2/8\pi$. As the neutrals lead the ions in the slow shock, Equation (3) implies that the magnetic pressure must drop. The velocity drop causes the ram pressure to drop, and so gas pressure must increase, which is shown in the third panel of Figure 6. Efficient line emission from CO and H₂ causes the temperature to quickly decrease, so to compensate the density must increase. This

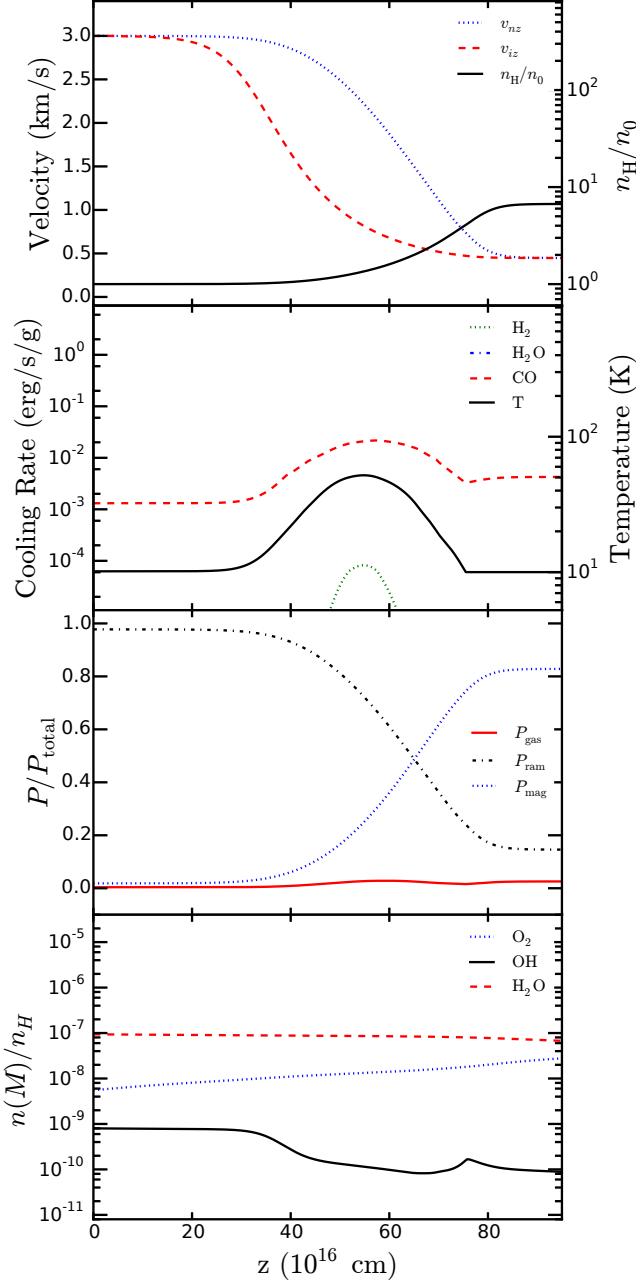


Figure 5. Profiles for a $v_s = 3 \text{ km s}^{-1}$ fast MHD shock propagating through a medium with initial number density $n_0 = 10^3 \text{ cm}^{-3}$ at 89.9° to a $10 \mu\text{G}$ magnetic field. The first panel shows the velocity and density profiles, the second panel shows the temperature and cooling rate profiles, the third panel shows the gas, ram and magnetic pressure profiles, and the fourth panel shows the abundances of selected oxygen molecules.

occurs smoothly in the $\sim 0.1 \times 10^{16} \text{ cm}$ after the initial jump, until the density reaches a plateau at a compression ratio of ~ 300 . The density finally settles as the neutral and ion velocities equalise.

While the velocity and density structural differences are large, the observational implications are sensitive to the temperature and cooling rate profiles shown in the second panels

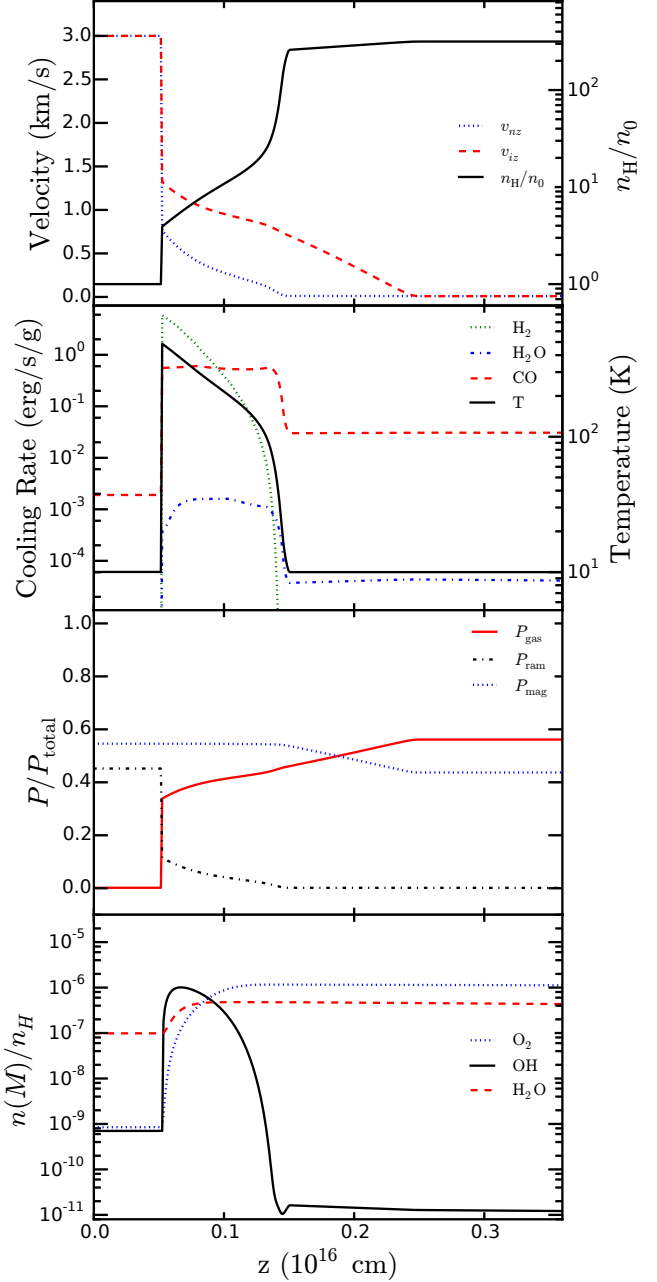


Figure 6. Same as Figure 5 but for a $v_s = 3 \text{ km s}^{-1}$ slow shock propagating through a medium with initial number density $n_0 = 10^3 \text{ cm}^{-3}$ at 30° to an $80 \mu\text{G}$ magnetic field.

of Figures 5 and 6. These panels show that the peak temperatures differ by an order of magnitude with the slow shock peaking at $\sim 487 \text{ K}$ and the fast shock peaking at $\sim 50 \text{ K}$. At this temperature, the fast shock causes CO emission only slightly above the background level. The slow shock is hot enough to emit significantly in lines of CO and H₂, and also in H₂O above the CO background emission. The fourth panels of Figures 5 and 6 also show that the slow shock drives more chemistry than the fast shock due to its high temperature. The strong H₂O emission in the slow shock is partially due to this increase in its abundance.

Following the pressure terms—in the third panels of Figures 5 and 6—through the shocks provides an intuitive understanding of the fundamental differences between fast and slow shocks. In the fast shock, the magnetic pressure (dotted lines) is higher in the postshock region than in the preshock region. As the gas pressure (solid lines) is negligible everywhere in this shock it is understood to be magnetically driven, where the high P_{mag} region pushes into the low P_{mag} region. The ion fluid is strongly coupled to the magnetic field, and so the ions are pushed forward ahead of the neutrals. This is why the ions lead the neutrals in the velocity profile. This situation is reversed in the slow shock, where a high gas pressure pushes the neutrals through the ions. In this case, the ion coupling to the magnetic field deforms it and increases the separation between field lines, which reduces the field strength.

Comparison of fluxes

The cooling discussed in Section 2.3 can be used to search for observational differences between the kinds of shocks. Integrating the cooling rate—middle panels of Figures 5 and 6—through the shocks gives the flux emitted in the direction of the shock normal. In Figure 7, we compare the CO, H₂ and H₂O fluxes of all the fast and slow shocks in Table 3.

The CO flux is similar between both kinds and across the velocity range. The H₂ flux is much more temperature sensitive and is therefore stronger in the slow shocks by 5 orders of magnitude at the lowest velocity and 1 order of magnitude at the highest. The H₂O flux is also stronger in the slow shock at all velocities.

Figure 7 shows that for slow shocks the CO and H₂ fluxes are within an order of magnitude of each other at all velocities. For fast shocks, however, the CO flux is always stronger by more than an order of magnitude. This feature holds at initial densities $n_0 = 10^2$ and 10^4 cm⁻³, though the magnitudes of the fluxes are lower and higher respectively by factors of 10 than the $n_0 = 10^3$ cm⁻³ case. This suggests that combining observations of flux from both molecules is a strong indicator of the kind of shock being observed.

Rotational lines

Figure 7 shows similar levels of CO flux for both fast and slow shocks at all the velocities considered here. However, the strength of the individual rotational lines that make up this flux is not expected to be the same given the higher temperatures that slow shocks reach. Here we estimate those line strengths using the non local thermodynamic equilibrium (LTE) radiative transfer code RADEX (van der Tak et al. 2007).

For a given radiating molecule, RADEX requires as input the density of H₂ as the collisional partner, the column density of the radiating molecule, the temperature and the linewidth. We consider 4 molecules with H₂ as the collisional partner: ¹²CO, ¹³CO, ortho-H₂O and para-H₂O. We use a ¹²CO to ¹³CO ratio of 61:1, well within the range of measurements given by Milam et al. (2005), and an ortho-to-para H₂O ratio of 3:1 as assumed in Section 2.3 for the cooling function.

We use RADEX in slab mode, and use density weighted

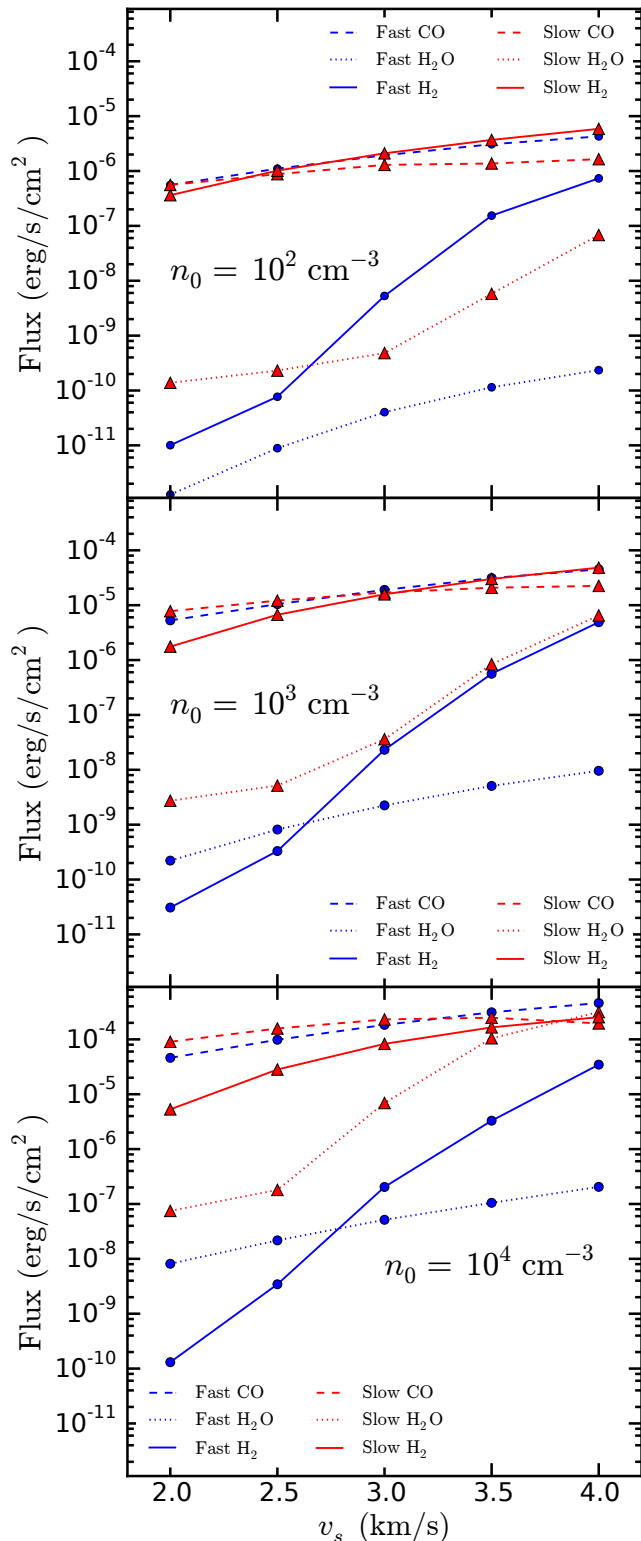


Figure 7. Energy flux contributions by different coolants in shocks of initial density $n_0 = 10^2$ cm⁻³ (top), $n_0 = 10^3$ cm⁻³ (middle) and $n_0 = 10^4$ cm⁻³ (bottom), and shock velocities $v_s = 2\text{--}4$ km s⁻¹. Blue circles refer to fast shocks and red triangles refer to slow shocks. Solid, dotted and dashed line types indicate whether the coolant is CO, H₂ or H₂O respectively.

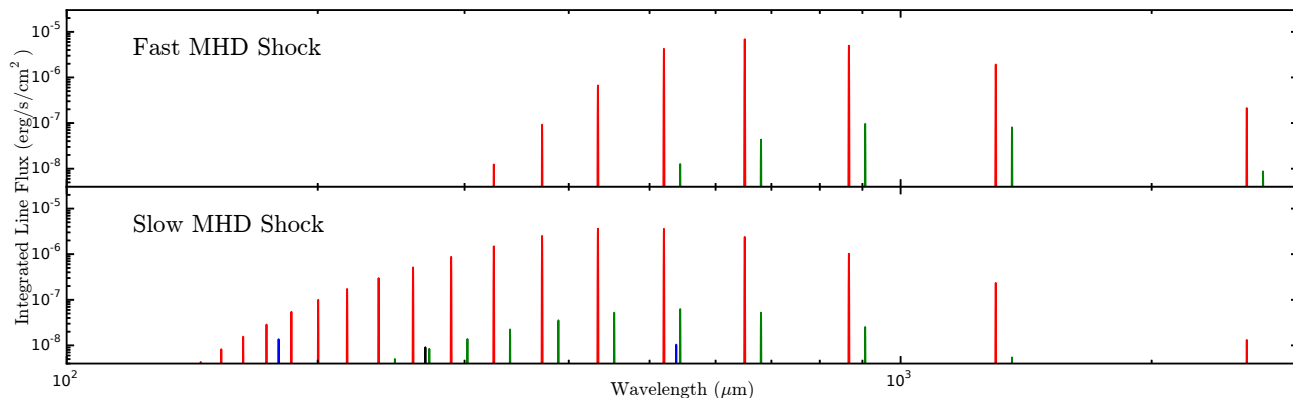


Figure 8. Estimates of integrated line fluxes from rotational lines of ^{12}CO (red), ^{13}CO (green), ortho- H_2O (blue) and para- H_2O (black) for the fast (top) and slow (bottom) shocks shown in Figures 5 and 6.

averages of the required inputs over appropriate slab definitions of the computed shocks. For slow shocks, we define multiple slabs in order to account for the complex temperature and density structure. While RADEX accounts for optical depth effects within each slab and outputs the optical depth for each rotational transition, the emission from a slab may be reabsorbed by the other slabs it has to pass to reach the observer. Hence estimates of line strengths from lines of high optical depth—such as the CO lines below $J = 5 \rightarrow 4$ —may not be reliable. Differences in the optical depth of particular lines in fast and slow shocks may have an observational effect. For example, Burkhardt et al. (2013) show that the slope of the spatial power spectrum derived from synthetic observations of $^{13}\text{CO } J = 2 \rightarrow 1$ in simulations of MHD turbulence is sensitive to the optical depth of this line. Furthermore, this slope could distinguish between sub- and super-Alfvénic turbulence. However, to relate the optical depth of a line emitting from dense postshock regions to that over a line of sight through a cloud requires knowledge of the spatial distribution of shock waves in the cloud, which is beyond the scope of this paper. Finally, we normalise the line strengths so that emission from each molecule from all its lines is equal to the fluxes given in Figure 7.

In Figure 8 we plot the line strengths as computed by RADEX for the fast and slow shocks shown in Figures 5 and 6. As expected, the higher temperature of the slow shock results in strong excitation of the high- J CO transitions of both isotopes. There are also excited H_2O lines in the slow shock that are negligible in the fast shock.

Any line of sight through a cloud will intersect multiple shocks propagating at different velocities, so we look for features in the spectra that hold across the velocity range. In Figure 9 we plot the line integrated fluxes for selected high- J lines of CO across the velocity and density ranges for fast and slow shocks. In all slow shocks, the dynamic range of these high- J lines of CO is much lower than in fast shocks. For example, the line ratio $\text{CO } J = 5 \rightarrow 4/10 \rightarrow 9$ for a fast shock is always greater than 30 times the ratio from the slow shock of the same velocity and density.

As line ratios don’t change if the line strengths are reduced by a constant factor, these distinguishing features will remain even though the shocks propagate in various directions with respect to the line of sight. Furthermore, any line

of sight through a turbulent cloud will cross multiple shock fronts. Emission from optically thin lines will be a simple addition of emission from each shock, retaining line ratio characteristics which therefore could be strong indicators of shock type.

The high temperatures reached within slow shocks allow H_2 cooling to become comparable to cooling by CO, as can be seen in Figure 7. The H_2 molecule has no dipole moment, and so this cooling is due to weak quadrupole emission. We can estimate the low lying pure rotational lines ($\nu = 0 \rightarrow 0$) of this emission using Figure 1 of Burton et al. (1992), which assumes the column of radiating H_2 is in LTE. For pure rotational lines S(0)-S(3), the line integrated fluxes emitted normal to the plane of the slow shock in Figure 6 are in the range $\sim 10^{-7}$ - 10^{-6} erg/cm²/s. These lines are strongly suppressed in gas below 100 K, and so the fast shock in Figure 5 produces negligible S(0)-S(3) line emission. This estimate shows that the pure rotational lines of H_2 could be an important diagnostic of shock type. However, the assumption of LTE doesn’t always hold and so to produce a more accurate prediction for H_2 rovibrational line emission the level populations would have to be computed in parallel with the shock flow variables and reaction rate equations, as is done for instance in the fast shock model of Gusdorf et al. (2008).

5 DISCUSSION

We have integrated the two-fluid MHD equations to obtain one dimensional time-independent fast and slow shock wave solutions. While two-fluid fast MHD shocks have been well studied (e.g. Draine 1986; Flower & Pineau Des Forêts 1998), two-fluid slow shocks have not been considered in molecular cloud conditions. Thus we use a simplified model in order to highlight the qualitative differences between the two kinds of shocks. Simplifications include restricting the chemical network to a small subset of reactions that influence the abundance of H_2O , as this is an important coolant in molecular gas. Gas-phase oxygen chemistry is well contained in the restricted network used here (Iglesias & Silk 1978) and so a richer network—such as that used in (Glover et al. 2010)—would not strongly affect H_2O production. We have not modeled how a variety of differ-

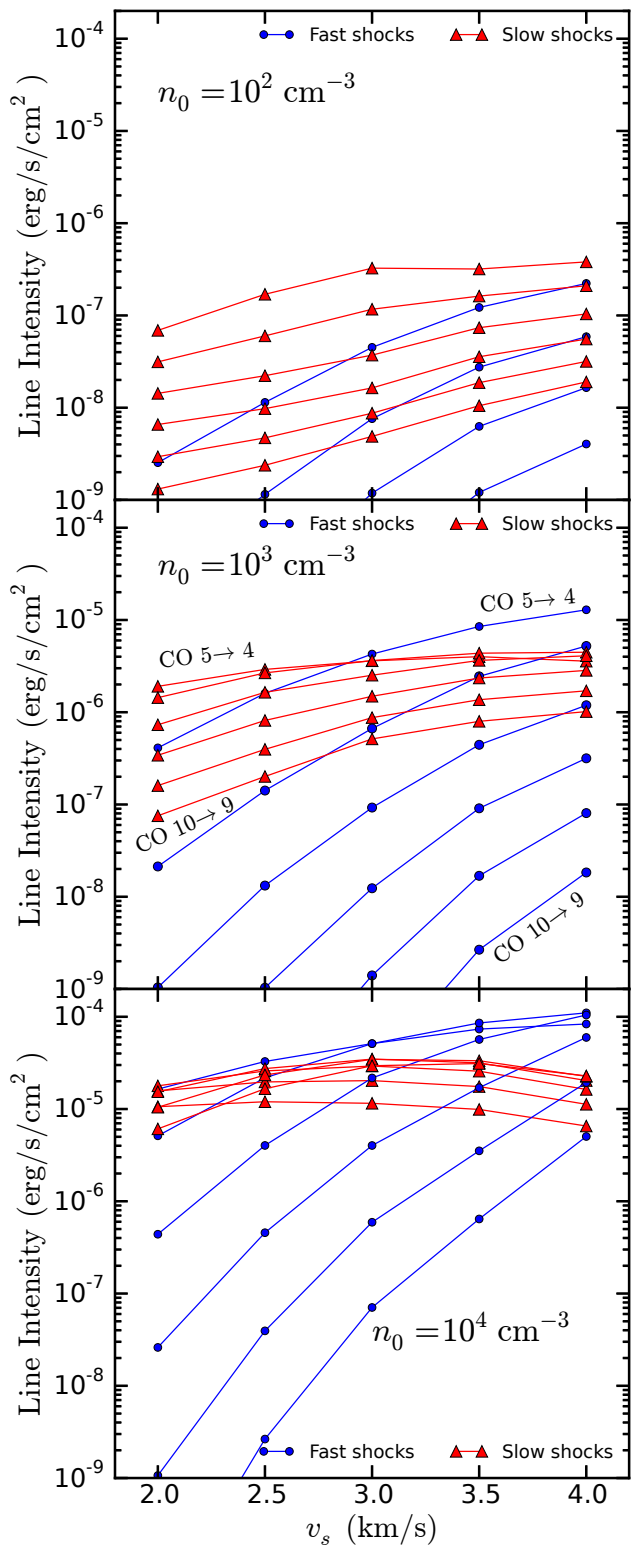


Figure 9. Integrated line intensities of CO rotational lines for fast (blue circles) and slow (red triangles) shocks with preshock densities $n_0 = 10^2 \text{ cm}^{-3}$ (top), $n_0 = 10^3 \text{ cm}^{-3}$ (middle) and $n_0 = 10^4 \text{ cm}^{-3}$ (bottom), and shock velocities $v_s = 2 - 4 \text{ km s}^{-1}$. The solid lines connect rotational lines of the same transition from $J = 5 \rightarrow 4$ to $J = 10 \rightarrow 9$.

ent initial abundances—which varies throughout a turbulent molecular cloud (Glover et al. 2010)—could affect the shock chemistry or cooling profiles. However, this will not change the general differences in structure between fast and slow shocks which is determined by whether the shock is driven by magnetic or gas pressure, respectively. Rotational line emission from H_2 could provide more observational diagnostics and has been computed in fast shock models by Lesaffre et al. (2013). In order to predict this emission accurately the level populations of the rovibrational states of H_2 have to be computed in parallel with the shock flow variables and reaction rate equations.

This work shows that fast and slow MHD shocks are structurally and observationally distinct. In Section 2.1 we noted that fast shocks increase the angle between the magnetic field and direction of propagation whereas slow shocks decrease this angle. In principle this effect could be observed in studies of the polarized thermal emission revealing the geometry of magnetic fields in molecular clouds. The study by Planck Collaboration et al. (2015) has shown that in high column density filaments the magnetic field tends to be perpendicular to the filament. Padoan et al. (2001) explain these filaments as dense postshock regions resulting from the collision of supersonic turbulent flows. This result precludes the possibility that the filaments contain the fast shocks most commonly modeled (e.g. Flower & Pineau Des Forêts 2010; Pon et al. 2012) in which the magnetic field is parallel to the shock front. Higher spatial resolution work of this kind could either detect the magnetic field bending across shock fronts or rule out the shock formation scenario of filaments. In Section 4 we showed that observations of high- J CO lines—above $J = 6 \rightarrow 5$ —could distinguish between fast and slow MHD shocks. Multiple transitions should simultaneously be observed to disentangle the possible shock models through the use of line ratios. In addition, velocity information from linewidths could be used to constrain the shock velocity of the model. Hence, useful observations would require spectral resolutions better than 1 km/s at the high- J CO lines (CO $J = 6 \rightarrow 5$ to $J = 10 \rightarrow 9$ lines lie in the frequency range $691.47\text{--}1151.99 \text{ GHz}$). In addition, the spatial resolution must be sufficient to avoid gas warmed by protostellar outflows or stellar winds. By way of example, we consider a recent observation that satisfies these criteria and show that slow shock signatures may be present.

Pon et al. (2015) (hereafter P15) present observations of CO $J = 8 \rightarrow 7$, $9 \rightarrow 8$ and $10 \rightarrow 9$ taken with the *Herschel* Space Observatory, towards four starless clumps within Galactic infrared dark clouds (IRDCs). These clumps were chosen because they lacked massive embedded protostars, avoiding confusion from outflows which could also create a warm gas component. The authors detect CO $J = 8 \rightarrow 7$ and $9 \rightarrow 8$ towards three of their clumps—named C1, F1 and F2—and give an upper limit for the $10 \rightarrow 9$ line. They compare these observations to PDR models at densities of 10^4 and 10^5 cm^{-3} , typical of IRDCs, and interstellar radiation fields of 1 and ~ 3 Habing. All of the PDR models underpredict the CO $J = 9 \rightarrow 8$ line, so the authors suggest that the dissipation of turbulence in low velocity shocks could account for these lines. Here we consider how fast and slow shocks similar to those modeled in this paper could account for these observations.

To convert the integrated line intensity ($\int T dv$) of P15

Table 4. CO high- J line luminosities for IRDCs (Pon et al. 2015) and selected shock models

Source	CO $J = 8 \rightarrow 7$ (10^{-14} erg/s/cm 2)	CO $J = 9 \rightarrow 8/8 \rightarrow 7$	CO $J = 10 \rightarrow 9/8 \rightarrow 7$
C1	1.26 ± 0.06	0.65 ± 0.07	$< 2.10 \pm 0.24$
F1	1.48 ± 0.09	0.94 ± 0.10	$< 2.20 \pm 0.29$
F2	1.19 ± 0.09	0.77 ± 0.10	$< 2.69 \pm 0.36$
Slow Shock Models			
(A)	1.66	0.51	0.27
(B)	1.75	0.80	0.58
Fast Shock Models			
(A)	1.19	0.16	0.03
(B)	4.10	0.25	0.06

Notes. The values used for the $J = 10 \rightarrow 9$ line from IRDCs are the suggested upper limits. Slow shocks A and B have shock velocities $v_s = 2 \text{ km s}^{-1}$ and 3.5 km s^{-1} respectively. Fast shocks A and B have shock velocities $v_s = 3.5 \text{ km s}^{-1}$ and 4.0 km s^{-1} respectively. All four shock models have preshock density $n_0 = 10^4 \text{ cm}^{-3}$.

to flux we use the formula

$$F = \frac{2k\Omega\nu^3}{c^3} \int T dv$$

where k is the Boltzmann constant, Ω is the beam area, ν is the frequency of the transition under consideration and c is the speed of light. The CO $J = 8 \rightarrow 7$, $9 \rightarrow 8$ and $10 \rightarrow 9$ transitions have rest frequencies of 921.80, 1036.91 and 1151.99 GHz and half power beam widths (HPBW) of 23, 20 and 19 arcseconds respectively. We use

$$\Omega = \frac{\pi}{4 \ln 2} (\text{HPBW})^2$$

to compute the beam area. Finally, we use the average of the detected line intensities for comparison (Column 8 of Table 3 in Pon15). For this set of values the line fluxes are shown in Table 4. The second column shows the CO $J = 8 \rightarrow 7$ line flux, while the third and fourth columns show the CO $J = 9 \rightarrow 8/8 \rightarrow 7$ and CO $J = 10 \rightarrow 9/8 \rightarrow 7$ line ratios respectively. The CO $J = 10 \rightarrow 9$ line was not detected in any of the clumps so we use the upper limits adopted in Pon15. This means that the CO $J = 10 \rightarrow 9/8 \rightarrow 7$ line ratio is an upper limit.

We also list in Table 4 the predicted values from selected slow and fast shocks by multiplying the RADEX intensities (Figure 9) by $\Omega/4\pi$ for the appropriate beam areas. The predicted value of the CO $J = 8 \rightarrow 7$ integrated intensity assumes the shock front faces the observer and fills the beam. We chose the models that give the closest CO $J = 8 \rightarrow 7$ line fluxes (Slow and Fast shock A in Table 4) as well as the shocks that give the closest CO $J = 9 \rightarrow 8/8 \rightarrow 7$ line ratios (Slow and Fast shock B in Table 4).

Slow shocks A and B have shock velocities $v_s = 2 \text{ km s}^{-1}$ and 3.5 km s^{-1} respectively. Fast shocks A and B have shock velocities $v_s = 3.5 \text{ km s}^{-1}$ and 4.0 km s^{-1} respectively. All four shock models have preshock density $n_0 = 10^4 \text{ cm}^{-3}$ which agrees well with typical densities of IRDCs. Fast shock A is the only shock that doesn't overpredict the observed integrated intensities, but the predicted integrated intensities of the other three models could be reduced to match the observations if the shock doesn't fill the beam. Hence the observed line flux of CO $J = 8 \rightarrow 7$ from these IRDCs can be explained by either fast or slow shocks.

The slow shocks generally fit the CO $J = 9 \rightarrow 8/8 \rightarrow 7$ line ratios better than the fast shocks, with the line ratio

from slow shock B (0.80) very close to the average of the ratio for all three clumps (~ 0.78). The predicted line ratio from fast shock B (0.25) is the largest predicted from all the fast shocks modeled, which still underpredicts the observed values by $\sim 3 - 4$ times. Hence the high temperatures produced in slow shocks are necessary to explain both the CO $J = 8 \rightarrow 7$ and $9 \rightarrow 8$ emission from these clumps. Combined with the inability of PDR models to explain these observations, we therefore suggest that a slow shock interpretation is favoured by the models in this paper.

6 CONCLUSIONS

The one dimensional time independent two-fluid MHD equations were numerically integrated to compare the structure of low-velocity fast and slow shocks in molecular clouds. Our simplified model includes the effects of the major coolants found in molecular clouds and follows the abundances of chemicals affecting the production of H $_2$ O in a simple chemical network. The solutions highlight important differences between fast and slow MHD shocks in molecular clouds. These shocks show strong differences in their velocity and density structure because of the different driving pressures behind the shock fronts. Fast shocks are driven by magnetic pressure while slow shocks are driven by gas pressure. This means that the thickness of fast shocks is set by the long ion-neutral collision timescale, whereas the thickness of slow shocks is set by the short neutral-ion collision timescale. The cooling timescale of the gas lies between these two and so peak temperatures in slow shocks are far higher than fast shocks of the same shock speed.

We showed that fast and slow shocks are observationally distinct and provided some example diagnostics. For instance, low lying pure rotational lines of H $_2$ contribute negligibly to the cooling in fast shocks, whereas they produce significant radiation from the warm gas in slow shocks. The non-LTE radiative transfer code RADEX was used to estimate line strengths of rotational transitions of ^{12}CO , ^{13}CO , ortho-H $_2\text{O}$ and para-H $_2\text{O}$. The higher temperatures of slow shocks excite the high- J transitions of ^{12}CO more than in fast shocks. Line ratios near these transitions show strong differences between fast and slow shocks across the velocity range and therefore may be strong indicators of shock type.

Anomalously strong high- J CO lines have been observed in nearby infrared dark clouds (Pon et al. 2015). The line ratios from these observations closely match slow shock predictions and are poorly fit by any of the fast shocks modeled here.

This suggests that simulations of MHD turbulence could gain observational predictions if the statistics of shock types were recorded. If the mixture of shock families is found to be sensitive to turbulence parameters—such as the driving mode, the kind of feedback included, Mach number variations and self-gravity—then shock signatures become observational probes of the turbulence. Combined with tracers of star formation like young stellar objects, shock signatures could then shed light on the influence of supersonic MHD turbulence on the character of star formation.

ACKNOWLEDGMENTS

The authors gratefully acknowledge discussions with Christoph Federrath and James Tocknell, and thank the referee for a prompt and stimulating report. This research was supported under Australian Research Council’s Discovery Projects funding scheme (project number DP120101792). AL was supported by an Australian Postgraduate Award.

REFERENCES

- Balsara D. S., 1996, *ApJ*, 465, 775
 Bergin E. A., Tafalla M., 2007, *ARA&A*, 45, 339
 Burkhart B., Lazarian A., Balsara D., Meyer C., Cho J., 2015, *ApJ*, 805, 118
 Burkhart B., Lazarian A., Ossenkopf V., Stutzki J., 2013, *ApJ*, 771, 123
 Burton M. G., Hollenbach D. J., Tielens A. G. G., 1992, *ApJ*, 399, 563
 Chapman J. F., Wardle M., 2006, *MNRAS*, 371, 513
 Crutcher R. M., 1999, *ApJ*, 520, 706
 Crutcher R. M., Troland T. H., Goodman A. A., Heiles C., Kazes I., Myers P. C., 1993, *ApJ*, 407, 175
 Crutcher R. M., Wandelt B., Heiles C., Falgarone E., Troland T. H., 2010, *ApJ*, 725, 466
 Draine B. T., 1986, *MNRAS*, 220, 133
 Draine B. T., Katz N., 1986, *ApJ*, 306, 655
 Falle S. A. E. G., Komissarov S. S., 2001, *J. Plas. Phys.*, 65, 29
 Federrath C., Klessen R. S., 2012, *ApJ*, 761, 156
 Federrath C., Klessen R. S., 2013, *ApJ*, 763, 51
 Flower D. R., Pineau Des Forêts G., 1998, *MNRAS*, 297, 1182
 Flower D. R., Pineau Des Forêts G., 2010, *MNRAS*, 406, 1745
 Glover S. C. O., Federrath C., Mac Low M.-M., Klessen R. S., 2010, *MNRAS*, 404, 2
 Gredel R., Lepp S., Dalgarno A., Herbst E., 1989, *ApJ*, 347, 289
 Gusdorf A., Cabrit S., Flower D. R., Pineau Des Forêts G., 2008, *A&A*, 482, 809
 Hollenbach D., McKee C. F., 1989, *ApJ*, 342, 306
 Iglesias E. R., Silk J., 1978, *ApJ*, 226, 851
 Kamenetzky J. et al., 2012, *ApJ*, 753, 70
 Kennel C. F., Blandford R. D., Coppi P., 1989, *J. Plas. Phys.*, 42, 299
 Larson R. B., 1981, *MNRAS*, 194, 809
 Larson R. L., Evans II N. J., Green J. D., Yang Y.-L., 2015, *ApJ*, 806, 70
 Lazarian A., Vishniac E. T., Cho J., 2004, *ApJ*, 603, 180
 Lesaffre P., Pineau des Forêts G., Godard B., Guillard P., Boulanger F., Falgarone E., 2013, *A&A*, 550, 106
 Lithwick Y., Goldreich P., 2001, *ApJ*, 562, 279
 Mac Low M.-M., Klessen R. S., 2004, *Reviews of Modern Physics*, 76, 125
 McElroy D., Walsh C., Markwick A. J., Cordiner M. A., Smith K., Millar T. J., 2013, *A&A*, 550, 36
 McKee C. F., Ostriker E. C., 2007, *ARA&A*, 45, 565
 Meyer C. D., Balsara D. S., Burkhart B., Lazarian A., 2014, *MNRAS*, 439, 2197
 Milam S. N., Savage C., Brewster M. A., Ziurys L. M., Wyckoff S., 2005, *ApJ*, 634, 1126
 Neufeld D. A., Kaufman M. J., 1993, *ApJ*, 418, 263
 Neufeld D. A., Lepp S., Melnick G. J., 1995, *ApJS*, 100, 132
 Padoan P., Juvela M., Goodman A. A., Nordlund Å., 2001, *ApJ*, 553, 227
 Pellegrini E. W. et al., 2013, *ApJ*, 779, L19
 Pety J., Falgarone É., 2000, *A&A*, 356, 279
 Planck Collaboration et al., 2015, *ArXiv e-prints*, 1502, 4123
 Pon A., Caselli P., Johnstone D., Kaufman M., Butler M. J., Fontani F., Jiménez-Serra I., Tan J. C., 2015, *A&A*, 577, A75
 Pon A., Johnstone D., Kaufman M., Caselli P., Plume R., 2014, *MNRAS*, 445, 1508
 Pon A., Johnstone D., Kaufman M. J., 2012, *ApJ*, 748, 25
 Smith M. D., Mac Low M.-M., Heitsch F., 2000a, *A&A*, 362, 333
 Smith M. D., Mac Low M.-M., Zuev J. M., 2000b, *A&A*, 356, 287
 Solomon P. M., Rivolo A. R., Barrett J., Yahil A., 1987, *ApJ*, 319, 730
 Stone J., Ostriker E., Gammie C., 1998, *ApJ*, 508, L99
 Tilley D. A., Balsara D. S., 2011, *MNRAS*, 415, 3681
 van der Tak F. F. S., Black J. H., Schöier F. L., Jansen D. J., van Dishoeck E. F., 2007, *A&A*, 468, 627
 Wagner A. F., Graff M. M., 1987, *ApJ*, 317, 423
 Wu C. C., 1987, *GeoRL*, 14, 668